SOFT X-RAY TOMOGRAPHY ON TFTR

G. Kuo-Petravic

Plasma Physics Laboratory, Princeton University

Princeton, NJ 08543 USA

PPPL--2555

DE89 006858

ABSTRACT

The tomographic method used for deriving soft x-ray local emissivities on TFTR, using one horizontal array of 60 soft x-ray detectors, is described. This method, which is based on inversion of Fourier components and subsequent reconstruction, has been applied to the study of a sawtooth crash. A flattening in the soft x-ray profile, which we interpret as an m=1 island, is clearly visible during the precursor phase and its location and width correlate well with those from electron temperature profiles reconstructed from electron cyclotron emission measurements [G. Kuo-Petravic, PPPL-2556]. The limitations of the Fourier method, due notably to the aperiodic nature of the signals in the fast crash phase and the difficulty of obtaining accurately the higher Fourier harmonics, are discussed.

1. INTRODUCTION

The technique of tomographic reconstruction from line integral variables to local variables has been applied to a wide range of problems using all conceivable kinds of beams whose absorption or emission by an object enables us to obtain valuable local information without disturbing the object itself. Over the past 10 years this technique has been applied to the emissivity of soft x-rays from tokamak plasmas [1-3]. Measurements of soft x-rays in tokamaks have indicated that emission follows closely the contours of magnetic surfaces. Because the tomographic technique is intrinsically capable of high spatial and time resolution, we have here a very important tool for following the perturbations of the plasma which are caused by various magnetohydrodynamic instabilities. In particular, we shall concentrate on the sawtooth instability, which is a common feature of ohmically and neutral-beam-heated tokamaks. The sawtooth oscillations are a series of $m = 0, n = 0$ relaxations which flatten the central electron temperature, T_e, profile. The relaxations are usually preceded by an $m = 1, n = 1$ mode called the precursor, where m and n are poloidal and toroidal mode numbers, respectively. Tomographic reconstruction of the $m = 1, n = 1$ precursor mode followed by the crash and successor modes is described here in order to better understand the mechanism causing the sawtooth oscillations.

2. EXPERIMENTAL SETUP

A soft x-ray pinhole camera with a horizontal view was installed on TFTR. The spatial separation of the diodes is approximately 2.5 cm. A total of 60 horizontal diodes with fast (up to 500 kHz) and slow digitization is available. These diodes allow the detection of x-rays in the range 0.5 to 30 keV. Figure 1 shows the layout of the detector system. A sampling rate of 100 kHz was usually used for the sawtooth which had $m = 1, n = 1$ frequencies of $\approx$10 kHz.

A data processing and tomographic reconstruction program TOMO, was written to run on the VAX at PPPL. For a given shot on the TFTR, a data file containing 60 channels of 8192 digitized data is made. Figure 2 shows a sample of the traces for 18 diodes viewing the central region of the plasma above and below the midplane. After checking for time synchronization and correcting for the gain and offset of all the channels, adjustment is made for any remaining intrinsic disparity in the interval of sawtooth activity. If we choose an interval, as shown in Fig. 2, which lies exclusively within the precursor of a sawtooth burst and which is long compared to the $m = 1, n = 1$ oscillation period, we can time average the signals from each channel and display this against the impact radius or chord, p, as shown in Fig. 3. The data show some variations which must be attributed to some remaining systematic calibration error or detector variations, for example, the nonuniform thickness of the beryllium filters in front of the diodes. To correct for this, we fit a cubic spline to the experimental points subject to a least squares criterion. We then renormalize the data points by the smoothed values given by the spline.

3. RECONSTRUCTION METHOD

By virtue of the symmetries in the tokamak configuration, we have a doubly periodic system in the toroidal and poloidal angles. The detectors are all in a poloidal plane at a given toroidal location. The geometry of the reconstruction is shown in Fig. 4, where p is the impact radius and ϕ the chord angle. These two parameters uniquely define the detector view. The purpose of the reconstruction is to find poloidal variations of the plasma emissivity $g(r,\theta)$,where r is the minor radius and θ the poloidal angle, given the integrated emissivities along the lines of sight of the detectors, $f(p,\phi)$. At the time this work was initiated there existed already a computer code for inversion at PPPL written by Sauthoff et al. [4]. This code had been tested extensively using computer generated line integrals from some assumed source emissivity. Therefore, after the data processing part of the x-ray data was completed in collaboration with A.W. Morris, we were able to test the following three inversion methods on real TFTR data. These three methods are very briefly described here:

(i) "SMALL M"— [5] is suitable for $m < 2$ only. This method differentiates the integral of Eq. (4), hence, it is highly sensitive to noise in the data. However, it has the advantage that it satisfies causality conditions, for when differentiating it only uses information from the annulus outside the position of interest. The basic limitation is its inability to adequately address constraints for higher m's near the center.

(ii)"CORMACK LOW M"—[5] This technique uses series expansion and is related to (i) in that it uses information only from the exterior of the positions of interest, but it uses

Tschebycheff polynomial kernals. The approach is applicable to higher m's, but is subject to noise at the center due to similar constraints as (i) above.

(iii) "ZERNICKE"—[5] This technique, again due to Cormack[6], expands the line integral function $f_m(p)$ in a set of basis functions in an effort to reduce noise susceptibility by building in compliance with the modal constraints. The penalty is the violation of causality, in that information from regions interior to the point of interest is used.

Both methods i) and ii) have been found to be excessively noisy. Only (iii), which performs a least squares fit on the input data, produces smoother results. It is precisely because of this that one should be very careful with the outputs of this inversion method, and examination of the data at all intermediate stages is advisable. In our particular application, the study of the sawtooth instability, it has been found that all the gross features may be described by the rapid rotation of a single hotspot. It is, therefore, not surprising that method (iii), which is based on poloidal harmonic expansion, proves to be most suitable since this comes closest to describing the physics of the problem. From now on we shall restrict our discussion to Cormack's method with Zernicke polynomials only.

For the sake of completeness we shall briefly reproduce here the results of Cormack[6] for the localised emissivity function $g(r,\theta)$ given the line integral functions $f(p,\phi)$.

$$f(p,\phi) = \int_{I(p,\phi)} g(r,\theta)\, dI, \tag{1}$$

where dI is an element of length along the chord. Since there is no plasma outside a certain radius, we can define a unit radius outside which there is no source of radiation and expand

in Fourier series:

$$g(r,\theta) = \sum_{m=0}^{\infty} [g_m^c(r)\cos(m\theta) + g_m^s(r)\sin(m\theta)], \tag{2}$$

and

$$f(p,\phi) = \sum_{m=0}^{\infty} [f_m^c(p)\cos(m\phi) + f_m^s(p)\sin(m\phi)]. \tag{3}$$

Cormack showed that it follows from these expansions that:

$$f_m^{c,s}(p) = 2\int_p^1 \frac{g_m^{c,s}(r)T_m(p/r)r}{(r^2-p^2)^{1/2}}\, dp, \tag{4}$$

and the solution is:

$$g_m^{c,s}(r) = -\frac{1}{\pi}\frac{d}{dr}\int_r^1 \frac{r f_m^{c,s}(p)T_m(p/r)}{(p^2-r^2)^{1/2}p}\, dp, \tag{5}$$

where $T_m(x) = \cos(m\cos^{-1}x)$ is the Tschebycheff polynomial of the first kind of degree m in x.

Cormack showed that if we choose a particular set of basis functions:

$$f_{ml}(p) = \frac{2}{(m+2l+1)}\sin[(m+2l+1)\cos^{-1}(p)], \tag{6}$$

where m and l are non-negative integers and $0 < p < 1$ in this interval, the functions form an orthogonal and complete set. Furthermore, if we insert

$$f_m^{c,s}(p) = 2\sum_{l=0}^{L} a_{ml}^{c,s}\sin[(m+2l+1)\cos^{-1}(p)] \tag{7}$$

into Eq.(5), we obtain the solution

$$g_m^{c,s}(r) = \sum_{l=0}^{L} a_{ml}^{c,s}(m+2l+1)R_{ml}(r), \tag{8}$$

where L+1 is the total number of terms in the expansion, $a_{ml}^{c,s}$ are the same expansion coefficients which appeared in Eq.(7) and $R_{ml}(r)$ is the Zernicke polynomial

$$R_{ml}(r) = \sum_{s=0}^{l} \frac{(-1)^s\,(m+2l-s)!\;r^{m+2l-2s}}{s!\;(m+l-s)!\;(l-s)!}. \tag{9}$$

The complete local emissivity function $g(r,\theta)$ can then be found by substitution of Eq.(8) into Eq.(2). Not only is this solution simple and elegant, but the use of the poloidal harmonic expansion has reduced the problem to a one-dimensional fit in p space. In general, we seek a fit to the data points $f(p,\phi)$:

$$f(p,\phi) = 2\sum_{m=0}^{M}\sum_{l=0}^{L}[a_{ml}^{c}\cos(m\phi) + a_{ml}^{s}\sin(m\phi)]\sin[(m+2l+1)\cos^{-1}p]. \tag{10}$$

The unknown coefficients $a_{ml}^{c,s}$ can now be found by a least squares procedure which requires the inversion of an $N \times L$ matrix, where N is the number of diodes. It is important to choose a good matrix inversion method, for the discretization of the problem as well as the inherent noise present in the system can result in considerable deviations from the original orthogonal basis functions. This can happen at any particular combination of N and L. The net result is that the basis functions become to some degree not linearly independent, the matrix becomes singular and large error amplification sets in. After examining a few matrix inversion packages provided by the online Math libraries, we have finally chosen the Singular Value Decomposition (SVD) [7] method for the inversion of the least squares fit matrix. An outstanding feature of the SVD method is that the statistical errors inherent in the data can be incorporated into the matrix inversion process such that the final result takes them into account and is more accurate as a result. In the SVD method, the input matrix A is decomposed into three matrices Σ, U, and V. The matrix Σ is diagonal with non-negative

diagonal entries which are called the singular values of A. During the inversion process, the singular values of the matrix appear explicitly. Small singular values may appear indicating that the basis functions are not linearly independent at the data points. When this happens, we choose to ignore this singular value if it is $< \tau\sigma_1$, where τ is the relative error of the data points and σ_1 is the maximum singular value. In so doing we have actually improved the effective condition number, which is the ratio of the maximum to the minimum singular values, and minimized error amplification.

In our present system with the horizontal camera alone, the chord angles, ϕ, covered by the diodes above and below the midplane span the range $68° < \phi < 89°$ and $-89° < \phi < -68°$ only. This is barely sufficient to distinguish an $m = 1$ mode and certainly is capable of none higher. We, therefore, have to invoke some additional mechanism to interpret the data. Fortunately, there is good evidence to suggest that the rotating "hotspot" model works reasonably well[7]. As a first approximation, therefore, we can relate the observed oscillations in time to variations in poloidal angle of the hotspot as it spins around. Instead of calculating directly the instantaneous spatial variations of emissivity, which would be possible if more than one array of detectors were available, we calculate here the time variations of emissivity in terms of a Fourier mode and its harmonics. It is important here to distinguish between the poloidal mode number m and the harmonics number h. The mode number is given by the number of hotspots:

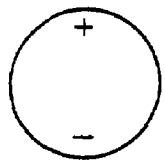

1 hotspot

mode m=1

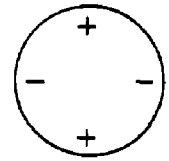

2 hotspot

mode m=2

In our analysis we treat one full oscillation period, T, of the signal, $e_p(t)$, at a time and form the Fourier integrals:

$$\bar{e}_p^c(\omega) = \int_{-T/2}^{T/2} e_p(t) \cos h(\omega t - \phi) dt, \tag{11}$$

and

$$\bar{e}_p^s(\omega) = \int_{-T/2}^{T/2} e_p(t) \sin h(\omega t - \phi) dt, \tag{12}$$

where $\omega = 2\pi/T$ and $h = 0, 1, 2, ...$ is the harmonic number.

The cosine and sine components $\bar{e}^c(\omega, p)$ and $\bar{e}^s(\omega, p)$ and their harmonics are separately input to the inversion package. The outputs are the Fourier components of the local emissivities $\bar{E}^c(\omega, r)$ and $\bar{E}^s(\omega, r)$ at frequency ω. To get back the local emissivity in physical space :

$$E(r,t) = \sum_{-\omega,0,\omega} [(\bar{E}^c(\omega, r) + \bar{E}^s(\omega, r)](\cos\omega t - i \ \sin\omega t). \tag{13}$$

$$\begin{aligned} E(r,t) &= E_0 + 2E_1^c(\omega_1)\cos\omega_1 t + 2E_1^s(\omega_1)\sin\omega_1 t + \cdots \\ &= E_0 + 2E_1\cos(\omega_1 t - \phi_1) + \cdots \end{aligned} \tag{14}$$

with $E_1 = ((E_1^c)^2 + (E_1^s)^2)^{1/2}$ and $tan\phi_1 = E_1^s/E_1^c$, where E_0 and E_1 are the $m = 1$, $h = 0$ and $m = 1$, $h = 1$ local emissivities, respectively.

4. RESULTS

Before proceeding to the analysis of data, we have to make some parameter tests. The most important is the convergence test to find the value of L, the number of basis functions required to reach convergence. General arguments would suggest $L \approx N$ for it is necessary to preserve any genuine fluctuations in signal at a scale length of approximately $1/N$. In practice, however, we need L to be smaller because the higher l terms in Eq.(7) tend to create noise at the large radius end owing to the non-exact cancellation of terms. Also, it should be borne in mind that a least squares method is guaranteed to give a smoothly varying profile however jagged the line integral input. For this reason, it is necessary to examine both the input and the output of the inversion process while varying all the parameters at one's disposal, such as the number of basis functions, L, the relative error of the data, τ, in the matrix inversion,and so on. In Fig. 5 we show an input data set consisting of $m = 1, h = 0$ Fourier integrals over one period of oscillation of the line integral data and this is fitted with L=6, 15, and 21 terms. It may be seen that the fit with L=6 does not reflect the change of curvature near the origin in the input while with 15 and 21 terms similar fits are obtained. The outputs of the three fits are shown in Fig. 5b. We conclude, therefore, that reasonable convergence may be obtained with $15 \leq L \leq 21$. Since we have a least squares method, the input data with statistical fluctuations are effectively replaced by a smoothed set resembling one of the fits of Fig. 5a. In other words, the output of the inversion we get (Fig. 6b)is the same as if our input data were smooth (Fig. 6a). This property is highly advantageous when the input is noisy.

As with any tomographic experiment, the first task after calibration is to simulate numerically the object of study under a set of simplifying assumptions. This tests not only code integrity, but also the geometry of the setup and finally the inversion method. In our case the detectors are sufficiently far away that the solid angle effects can be neglected. It is then easy to compute the line integral intensities of a rotating source with a given mode number m. Figure 7 shows the comparison of local emissivities given by the source and by inversion from computed line integrals for both the $m = 1, h = 1$ and $m = 2, h = 1$ cases. Such curves help us distinguish between $m = 1$ and $m = 2$ modes by the behavior near the center. Eventually study of the simulated emissions can even lead to a way of distinguishing structures with or without magnetic islands.

To obtain the Fourier integrals, we need to analyse the wave train cycle by cycle if the zeros of the oscillation can be determined. A cursory glance at Fig. 2 shows that the region near the $q = 1$ surface, where q is the safety factor, suffers the least change in the steady-state value during the crash as matter is expelled from the inside to the outside of the $q = 1$ surface. Figure 8a shows such a typical waveform. Here we can discern the end of the precursor phase leading to a sharp peak at the start of the crash phase and finally the beginning of the successor phase. To eliminate the steady-state portion of the waveform, we process the signal through a numerical low pass filter which replaces each point by a weighted average of a specific number of its neighbors on either side: this is shown by the solid curve. Figure 8b shows the residue when the time-averaged points are subtracted from the original signal. From this we derive eight oscillation periods(windows) which are analysed separately. In Fig. 9 we show the $m = 1, h = 0$ outputs of the inversion for all the windows. For $h = 0$

the Fourier integration of Eqs. (11) and (12) amounts to an average over one period of the steady level in the window for the cosine part and zero for the sine part. After the $h = 0$ portion has been subtracted from the signal, we form the $h = 1$ cosine and sine integrals. These measure that part of the perturbation which corresponds to an oscillation of frequency $\omega_1 = 2\pi/T$. Three distinct types of oscillations may be discerned:

(a) Precursor phase, windows (i), (ii), and (iii): This phase exhibits an almost steady-state oscillation over as long as 100 msec with the frequency decreasing slightly with time. These distributions are also the most reproducible from window to window. The $h = 1$ distribution shows a confinement of the "hotspot" in the range of $5 < r < 25$ cm, peaking at $r \approx 7$ cm.

(b) Crash phase, windows (iv):

In window (iv) the $h = 0$ distribution is no longer that of the precursor type for there is hollowness in the center. The $h = 1$ distribution is characterised by a broadening of the peak showing movement of matter out to larger radii. We conclude that the crash takes place over a time of half-rotational period or less, that is $\leq 50\mu$sec.

(c) Successor phase, windows (v), (vi), (vii), and (viii):

The average emissivity as given by the $h = 0$ distribution is still showing hollowness and the $h = 1$ distribution is double peaked.

In Figs. 10 and 11 we show the outputs for $m = 1, h = 1$ and $m = 1, h = 2$, respectively, for all windows. Combining the harmonic components according to Eq. (14), we get the total local emissivities E which are shown as contours and as 3-D plots in Fig. 12 and Fig. 13, respectively. An m=1 rotating island is clearly discernible in the precursor phase.

We are able to compare the position and the width of this island with that from electron temperature measurements from electron cyclotron emission (ECE), which viewed the same poloidal plane and the same sawtooth sequence [8]. Both the island location as well as island width agree to within 5%.

5. CONCLUSIONS

Since the precursor oscillations occur with great regularity, it is reasonable to expect the Fourier method to work rather well at least in this regime. The fact that we have good agreement between the soft x-ray and the ECE measurements is very reassuring for it validates both methods of analysis. Although purists would argue that there is no *a priori* reason why the location of an $m = 1$ island in soft x-ray emissivity should coincide with that of electron temperature and that cases have been seen in TFTR where the two differ by 10 or 20% [9], this is still a small difference. Until these cases are studied one can say that the two methods are at least accurate to this extent. While the Fourier inversion method works well for the precursor phase, the crash phase is much harder to treat for there are rapid changes on a time scale shorter than the rotation period. The hotspot follows a rapid helical motion with varying radii and the signal deviates far from a sinusoidal form showing the presence of high harmonics. Under these conditions it is difficult even to decide on the period because the phenomenon is strictly aperiodic. Therefore, the use of a Fourier method, which assumes the existence of periodic boundaries, is strictly invalid. Because of the small number of data points, the Fourier integrals become inaccurate for any h higher than 2. The crash phase is, therefore, poorly represented by this method. The oscillations in the

successor show reasonable periodicity though the signals are smaller in intensity. We expect our results to be reasonably accurate in this phase again.

ACKNOWLEDGMENTS

I am very grateful to Drs. A.W. Morris, N.R. Dauthoff, and K.M. McGuire who have all made very significant contributions to this work.

This work supported by the U.S. DOE Contract No. DE-AC02-76-CHO-3073.

REFERENCES

[1] R.S. GRANETZ, and J.F. CAMACHO, Nucl. Fusion **25** (1985) 727.

[2] D.J. CAMPBELL et al., Nucl. Fusion **26** (1986), 1085.

[3] A.W. EDWARDS et al., Phys. Rev. Lett. **57** (1986), 210.

[4] N.R. SAUTHOFF, K.M. McGUIRE, and S.von GOELER, Rev. Sci. Instrum. **8** (1986) 57.

[5] N.R. SAUTHOFF and S. von GOELER, IEEE Trans. Plasma Sci. **7** (1979) 141.

[6] A.M. CORMACK, J. of Appl. Phys. **35** (1964) 2908.

[7] G.E. FORSYTHE, M.A. MALCOLME, and B.M. CLEVE, Computer Methods for Mathematical Computations, Prentice Hall, New York (1977). For implementation of SVD Algorithm, see EISPACK LIB.

[8] G. KUO-PETRAVIC, Princeton Plasma Physics Laboratory Report No. PPPL-2556 (1988).

[9] K.M. McGUIRE, private communication.

FIGURE CAPTIONS

Figure 1. Horizontal x-ray imaging system on TFTR.

Figure 2. Raw data from 20 diodes above and below the midplane in the time range 4.837-4.84 seconds.

Figure 3. Time-averaged signals of diodes in the range 4.8-4.83 seconds as a function of chord p. This time range shows only precursor sawtooth oscillations and is used for calibration of the diodes.

Figure 4. Geometry of the inversion theory defining the chord or impact parameter p and the angle between the chord and the x-axis ϕ. These two parameters uniquely define the line of view $I(p, \phi)$.

Figure 5.

(a) Least squares fits with $L = 6, 15, 21$ on an input data set.

(b) Example of a convergence test. Several local emissivity curves are shown which differ in the number of terms L used in the basis function expansion of Eq.(7).

Figure 6.

(a) An artificially smoothed input data set derived from Fig. 5a.

(b) Output of (a) with $L = 15$.

Figure 7. Local emissivity curves from simulated rotating $m = 1, h = 1$ and $m = 2, h = 1$ sources and computed values from inversion using simulated line integrals.

Figure 8.

(a) Signal from a diode(H-06) viewing mostly near the $q = 1$ surface and a smoothed curve averaged from neighboring 8 points.

(b) Signal after subtraction of steady-state values, that is, difference of the 2 curves in Fig.9a.

Figure 9. The $m = 1, h = 0$ local emissivity E_0 for all windows.

Figure 10. The $m = 1, h = 1$ local emissivity E_1 for all windows.

Figure 11. The $m = 1, h = 2$ local emissivity E_2 for all windows.

Figure 12. The contour plots for $E(r, t)$ for all windows.

Figure 13. Ths 3-D plots for $E(r, t)$ for all windows.

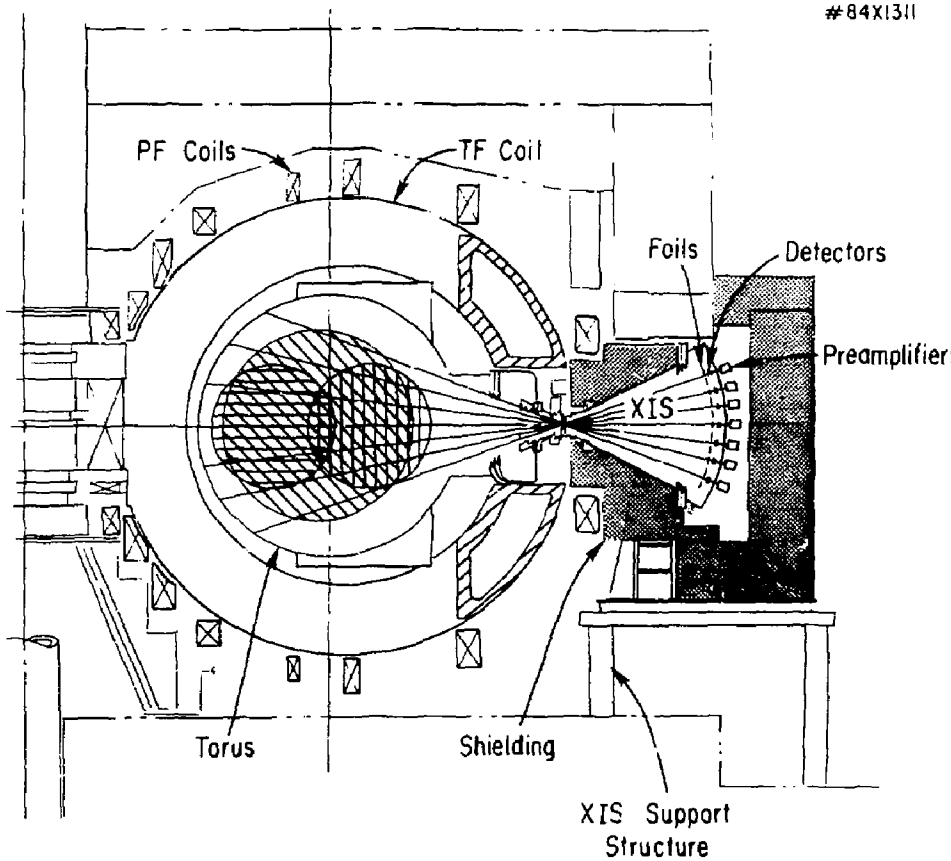
#84X1311
PF Coils
TF Coil
Foils
Detectors
Preamplifiers
XIS
Torus
Shielding
XIS Support
Structure

Fig. 1

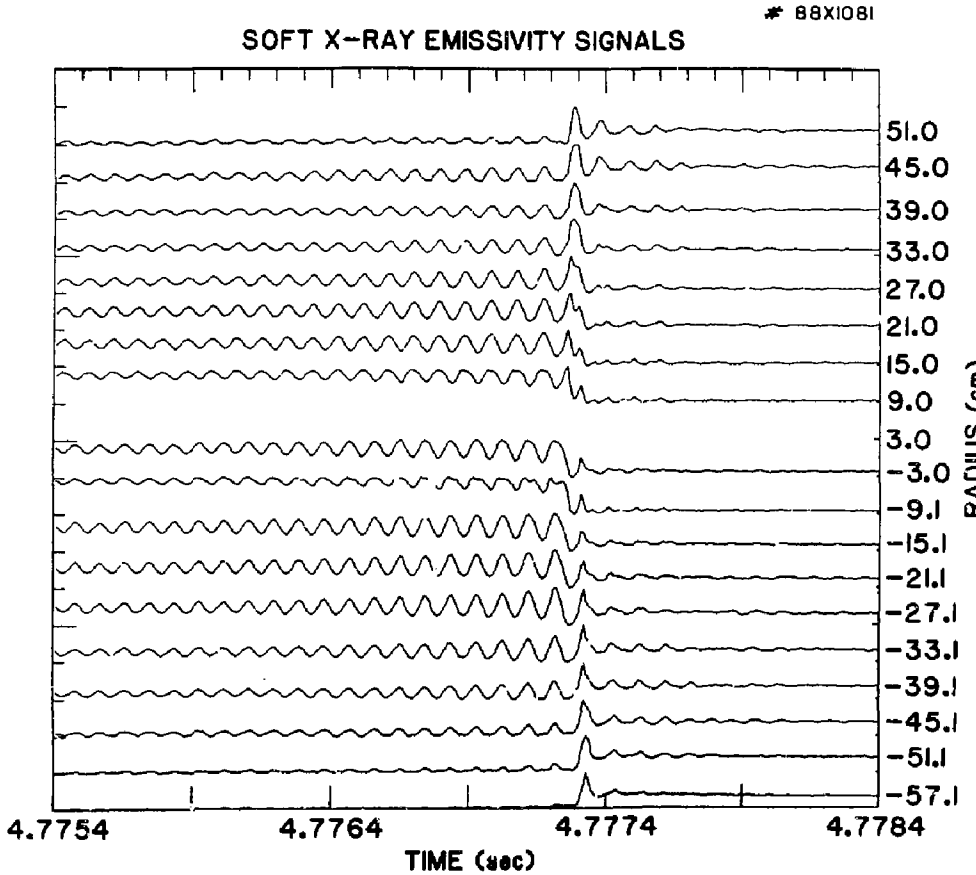
#88X1081
SOFT X-RAY EMISSIVITY SIGNALS
51.0
45.0
39.0
33.0
27.0
21.0
15.0
9.0
3.0
-3.0
-9.1
-15.1
-21.1
-27.1
-33.1
-39.1
-45.1
-51.1
-57.1
RADIUS (cm)
4.7754
4.7764
4.7774
4.7784
TIME (sec)

Fig. 2

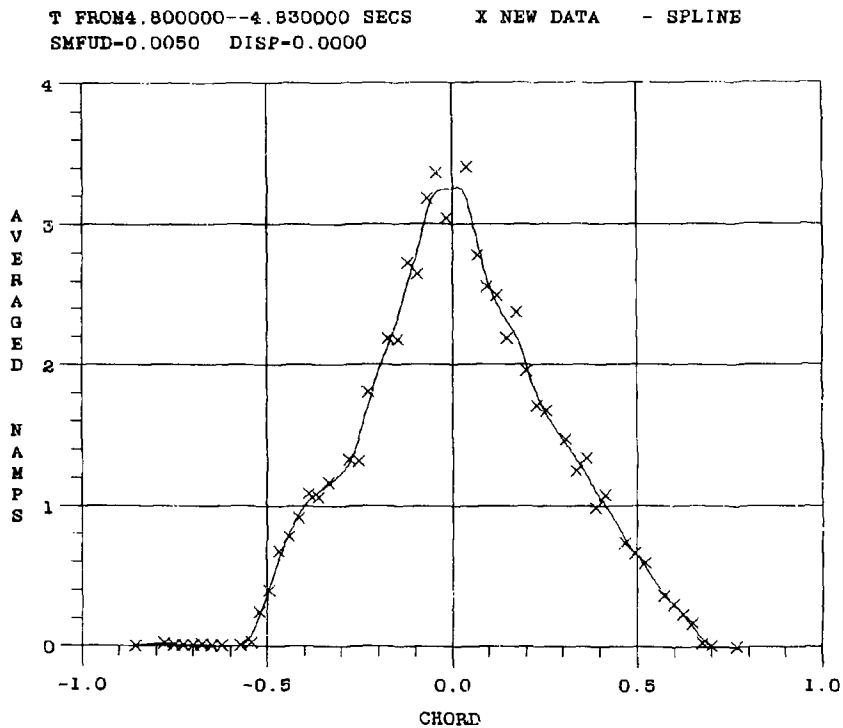
T FROM4.800000--4.830000 SECS X NEW DATA - SPLINE
SMFUD-0.0050 DISP-0.0000
AVERAGED NAMPS
CHORD
4
3
2
1
0
-1.0
-0.5
0.0
0.5
1.0

Fig. 3

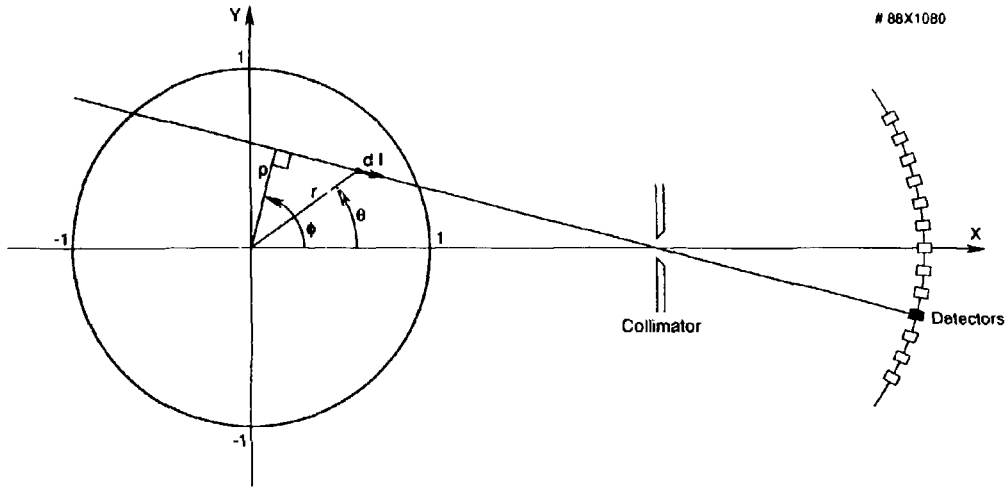

Fig. 4

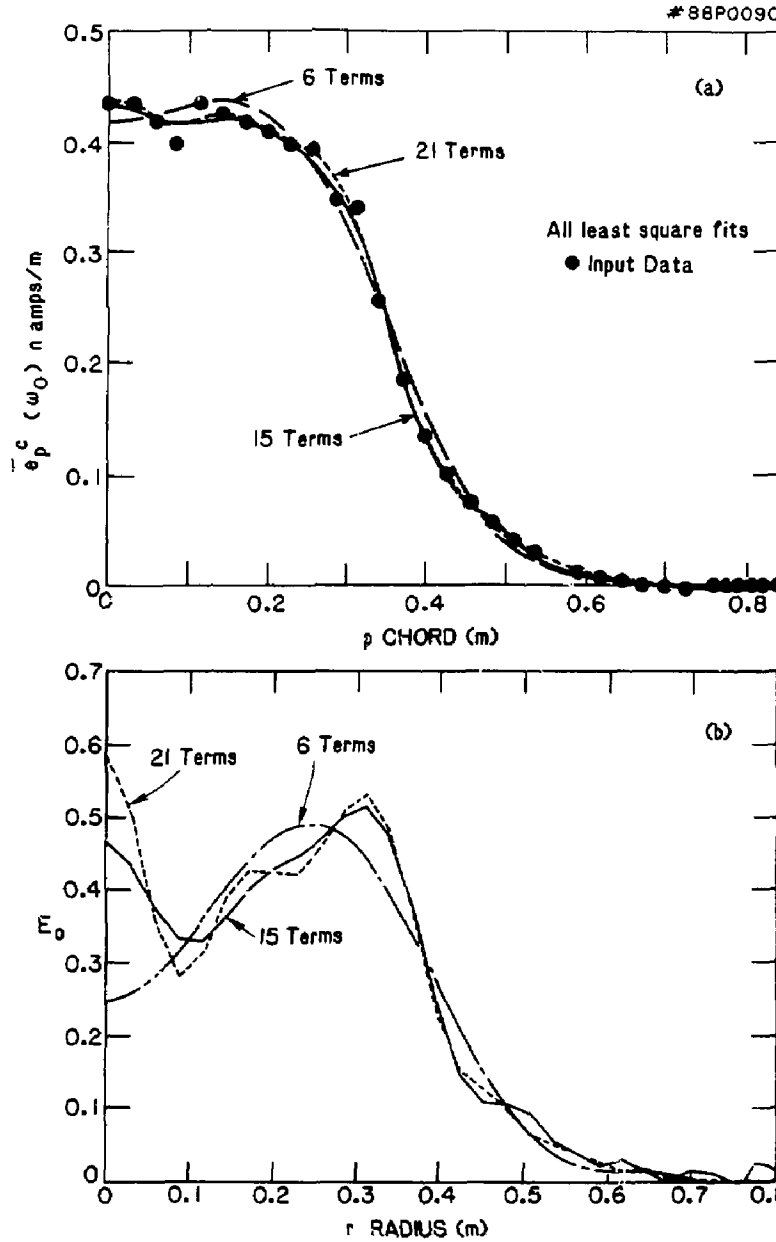
#88P0090
(a)
6 Terms
21 Terms
15 Terms
All least square fits
Input Data
$\bar{e}_p^c(\omega_0)$ n amps/m
p CHORD (m)
(b)
21 Terms
6 Terms
15 Terms
m_0
r RADIUS (m)

Fig. 5

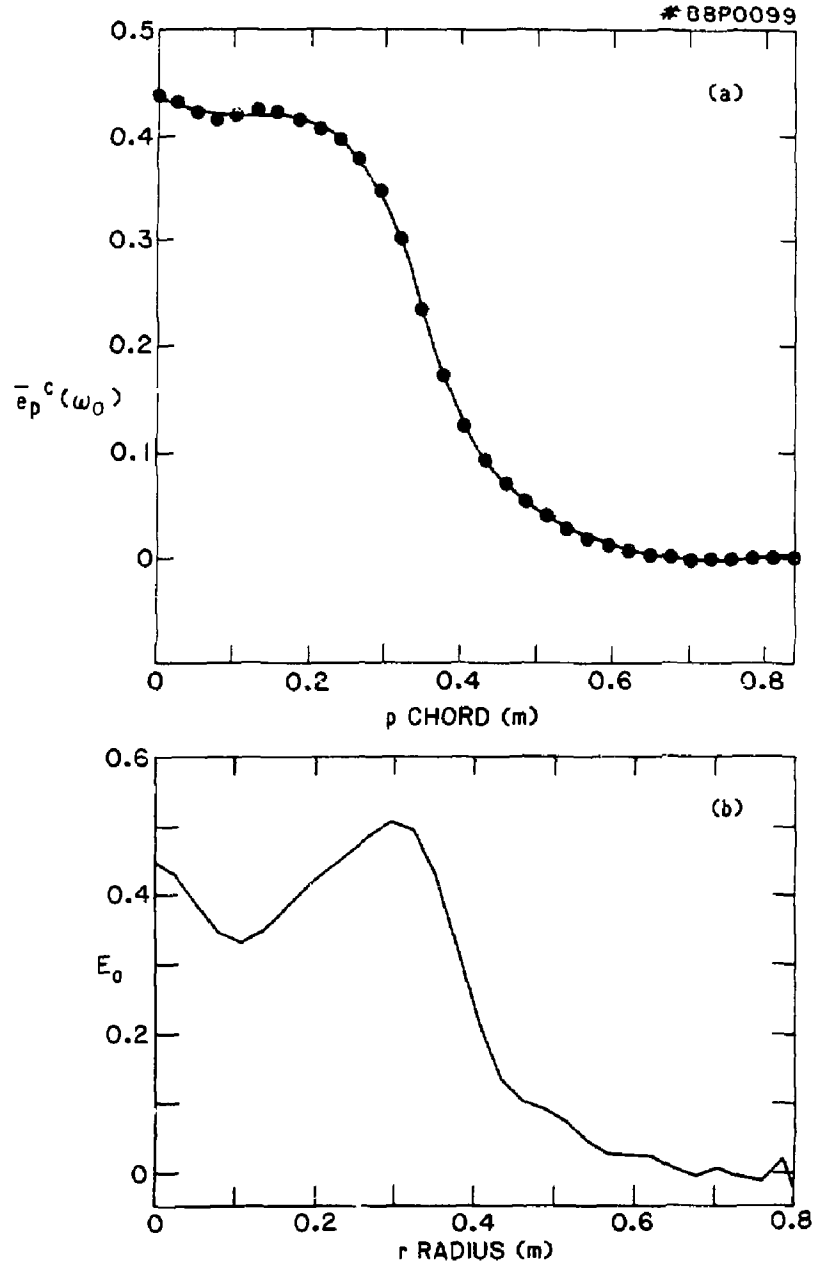
#88P0099
(a)
0.5
0.4
0.3
0.2
0.1
0
$\bar{e}_p{}^c(\omega_0)$
0
0.2
0.4
0.6
0.8
p CHORD (m)
(b)
0.6
0.4
0.2
0
E_0
0
0.2
0.4
0.6
0.8
r RADIUS (m)

Fig. 6

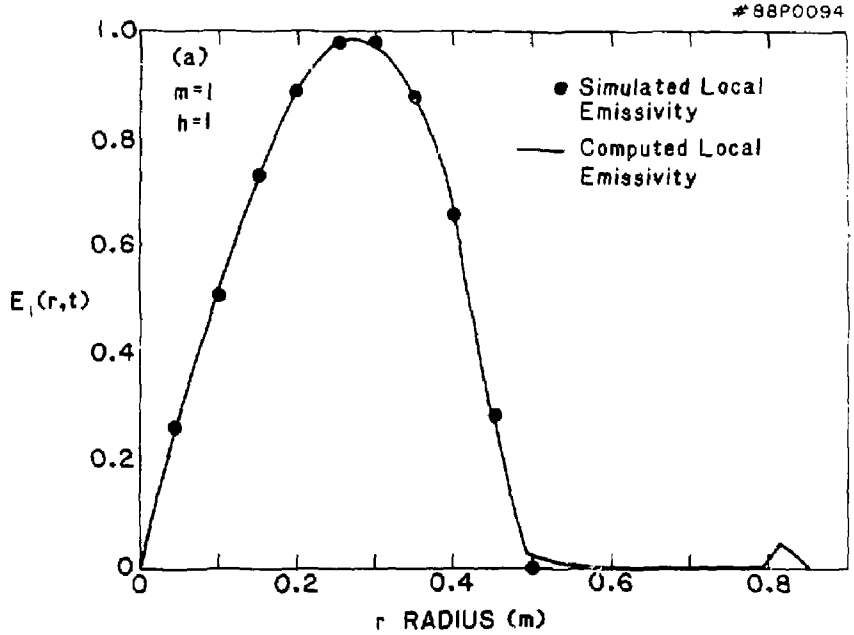
(a)
m=1
h=1
● Simulated Local Emissivity
— Computed Local Emissivity
$E_1(r,t)$
1.0
0.8
0.6
0.4
0.2
0
0
0.2
0.4
0.6
0.8
r RADIUS (m)

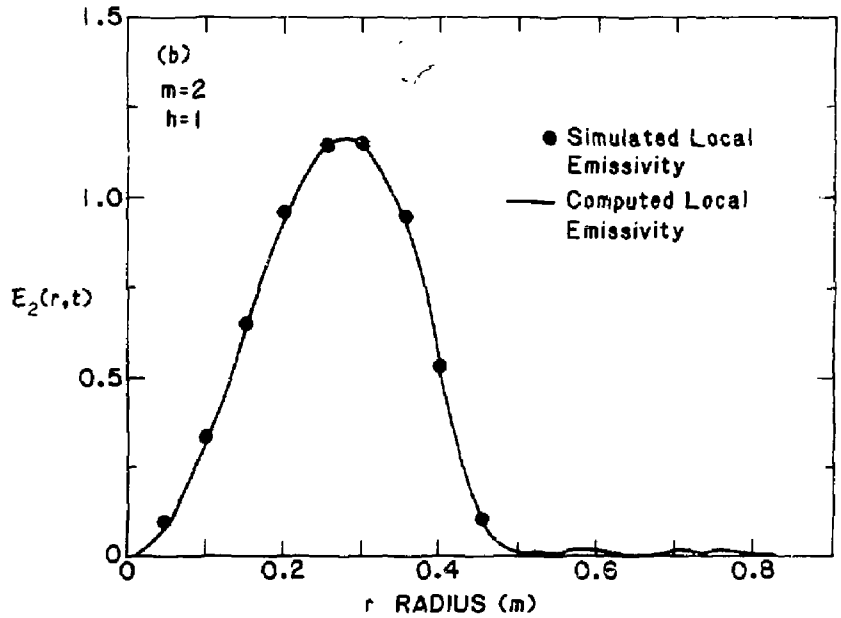
(b)
m=2
h=1
● Simulated Local Emissivity
— Computed Local Emissivity
$E_2(r,t)$
1.5
1.0
0.5
0
0
0.2
0.4
0.6
0.8
r RADIUS (m)

Fig. 7

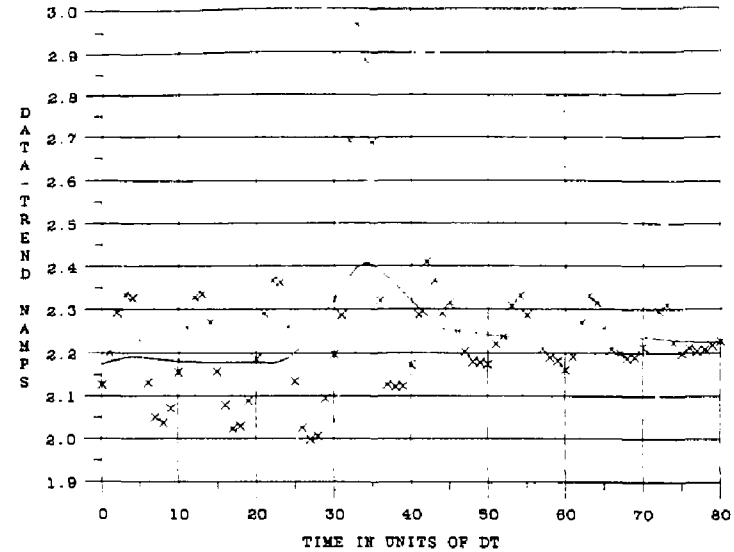
3.0
2.9
2.8
2.7
2.6
2.5
2.4
2.3
2.2
2.1
2.0
1.9
DATA-TREND NAMPS
0
10
20
30
40
50
60
70
80
TIME IN UNITS OF DT
T FROM4.838540--4.839340 SECS

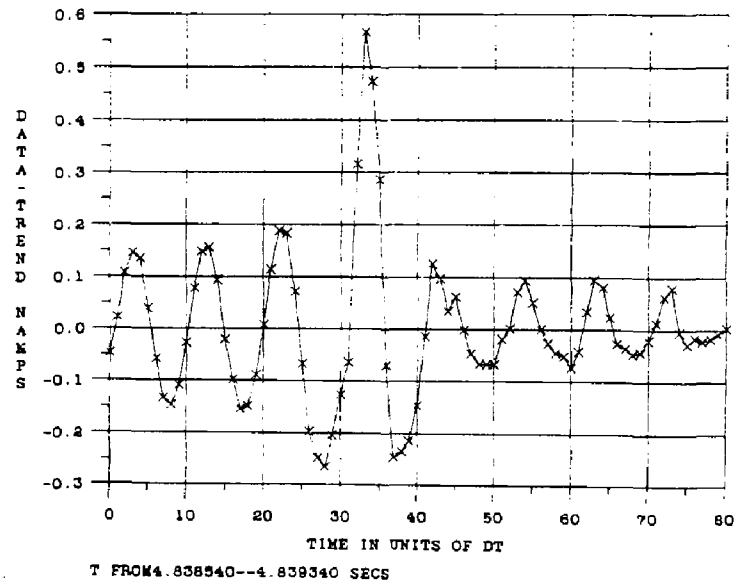
0.6
0.5
0.4
0.3
0.2
0.1
0.0
-0.1
-0.2
-0.3
DATA-TREND NAMPS
0
10
20
30
40
50
60
70
80
TIME IN UNITS OF DT
T FROM4.838540--4.839340 SECS

Fig. 8

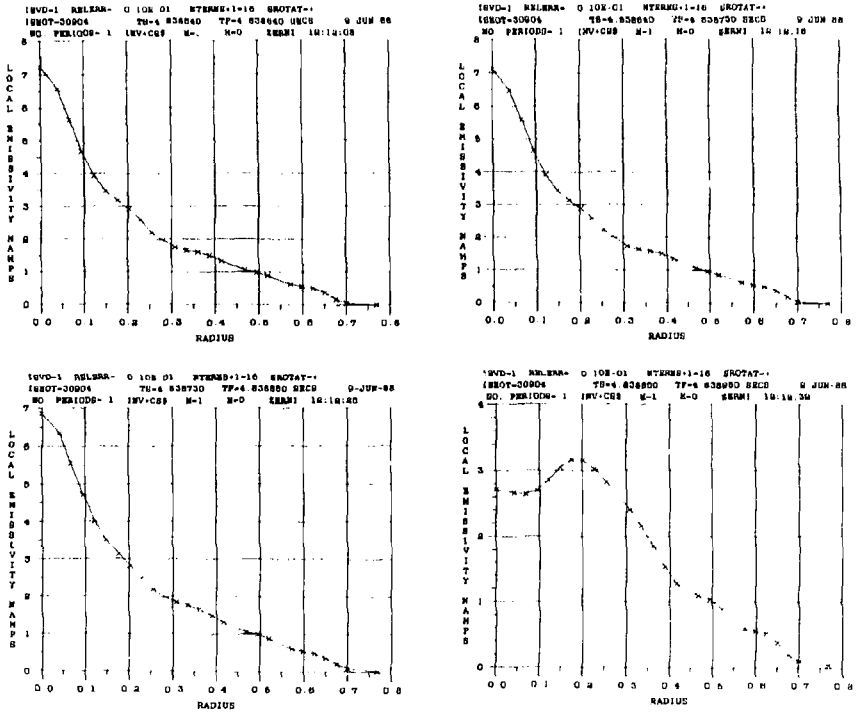

Fig. 9a

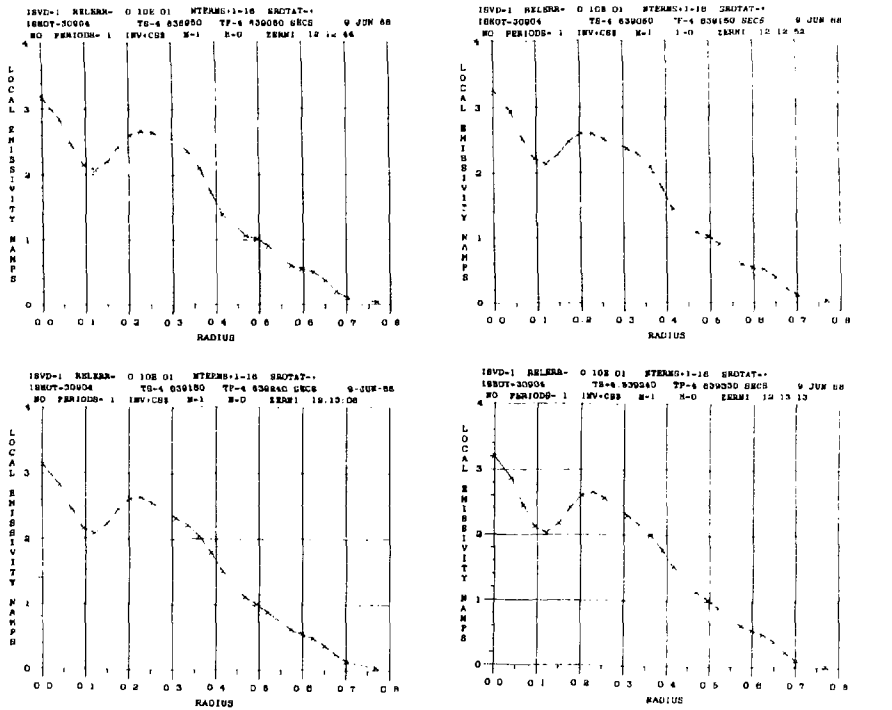
ISVD=1 RELERR= 0 10E 01 NTERMS=1-16 SROTAT=+
ISROT-30904 TS-4 639050 TF-4 639080 SECS 9 JUN 88
NO PERIODS= 1 INV+CBS N=1 N=0 TERMI 12 12 44
LOCAL EMISSIVITY MAPS
RADIUS
ISVD=1 RELERR= 0 10E 01 NTERMS=1-16 SROTAT=+
ISROT-30904 TS-4 639150 TF-4 639180 SECS 9 JUN 88
NO PERIODS= 1 INV+CBS N=1 N=0 TERMI 12 12 53
LOCAL EMISSIVITY MAPS
RADIUS
ISVD=1 RELERR= 0 10E 01 NTERMS=1-16 SROTAT=+
ISROT-30904 TS-4 639150 TF-4 639240 SECS 9-JUN-88
NO PERIODS= 1 INV+CBS N=1 N=0 TERMI 12:13:08
LOCAL EMISSIVITY MAPS
RADIUS
ISVD=1 RELERR= 0 10E 01 NTERMS=1-16 SROTAT=+
ISROT-30904 TS-4 639240 TF-4 639330 SECS 9 JUN 88
NO PERIODS= 1 INV+CBS N=1 N=0 TERMI 12 13 13
LOCAL EMISSIVITY MAPS
RADIUS

Fig. 9b

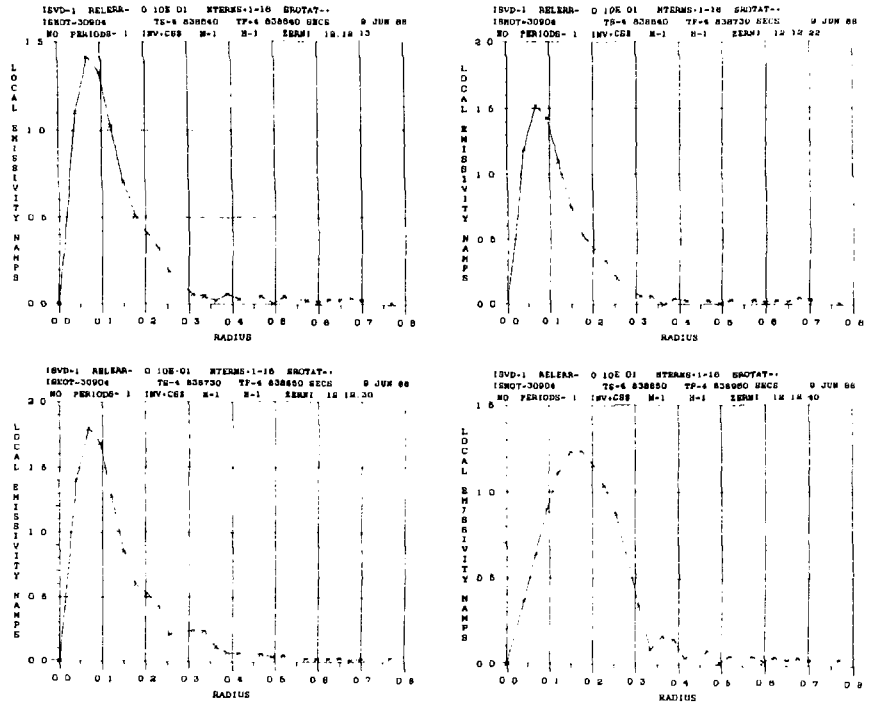
ISVD-1 RELERR- 0 10E 01 NTERMS-1-16 SROTAT--
ISNOT-30904 TS-4 838640 TF-4 838640 SECS 9 JUN 88
NO PERIODS- 1 ISV-CSS M-1 N-1 ZERNI 12 12 13
ISVD-1 RELERR- 0 10E 01 NTERMS-1-16 SROTAT--
ISNOT-30904 TS-4 838640 TF-4 838730 SECS 9 JUN 88
NO PERIODS- 1 ISV-CSS M-1 N-1 ZERNI 12 12 22
ISVD-1 RELERR- 0 10E-01 NTERMS-1-16 SROTAT--
ISNOT-30904 TS-4 838730 TF-4 838850 SECS 9 JUN 88
NO PERIODS- 1 ISV-CSS M-1 N-1 ZERNI 12 12 30
ISVD-1 RELERR- 0 10E 01 NTERMS-1-16 SROTAT--
ISNOT-30904 TS-4 838850 TF-4 838960 SECS 9 JUN 88
NO PERIODS- 1 ISV-CSS M-1 N-1 ZERNI 12 12 40
LOCAL EMISSIVITY MAMPS
RADIUS

Fig. 10a

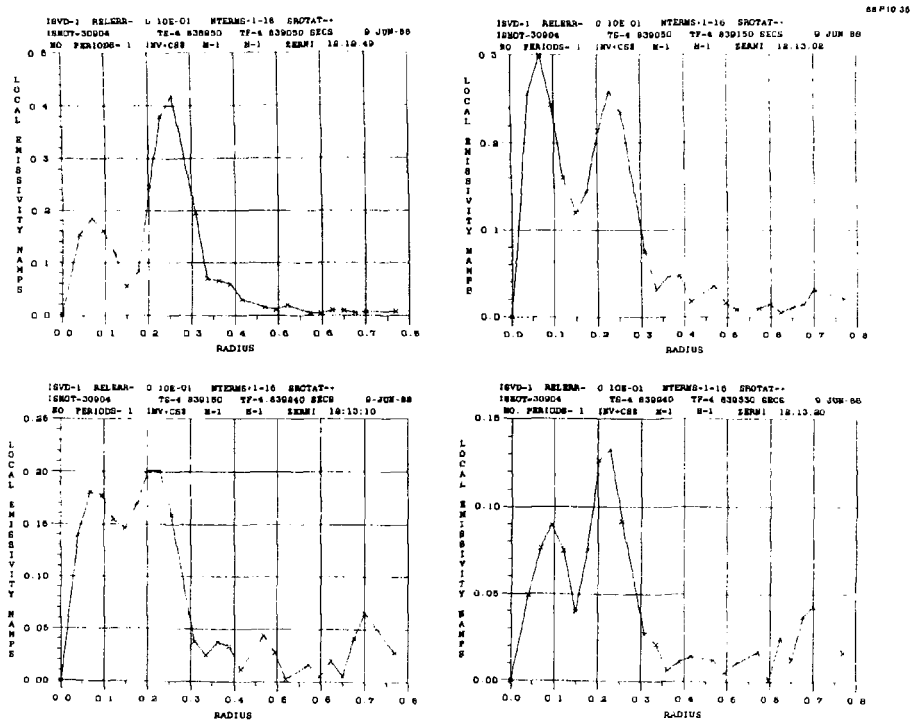
ISVD=1 RELERR= 0 10E-01 NTERMS=1-16 SROTAT=-
ISHOT=30904 TS=4 839050 TF=4 839150 SECS 9 JUN 88
NO. PERIODS= 1 INV=CSS M=1 N=1 SEAM1 18.13.02
LOCAL EMISSIVITY MAMPS
RADIUS
ISVD=1 RELERR= 0 10E-01 NTERMS=1-16 SROTAT=-
ISHOT=30904 TS=4 839050 TF=4 839150 SECS 9 JUN 88
NO. PERIODS= 1 INV=CSS M=1 N=1 SEAM1 18.13.02
LOCAL EMISSIVITY MAMPS
RADIUS
ISVD=1 RELERR= 0 10E-01 NTERMS=1-16 SROTAT=-
ISHOT=30904 TS=4 839150 TF=4 839440 SECS 9-JUN-88
NO. PERIODS= 1 INV=CSS M=1 N=1 SEAM1 18:13:10
LOCAL EMISSIVITY MAMPS
RADIUS
ISVD=1 RELERR= 0 10E-01 NTERMS=1-16 SROTAT=-
ISHOT=30904 TS=4 839440 TF=4 839530 SECS 9 JUN 88
NO. PERIODS= 1 INV=CSS M=1 N=1 SEAM1 18.13.30
LOCAL EMISSIVITY MAMPS
RADIUS

Fig. 10b

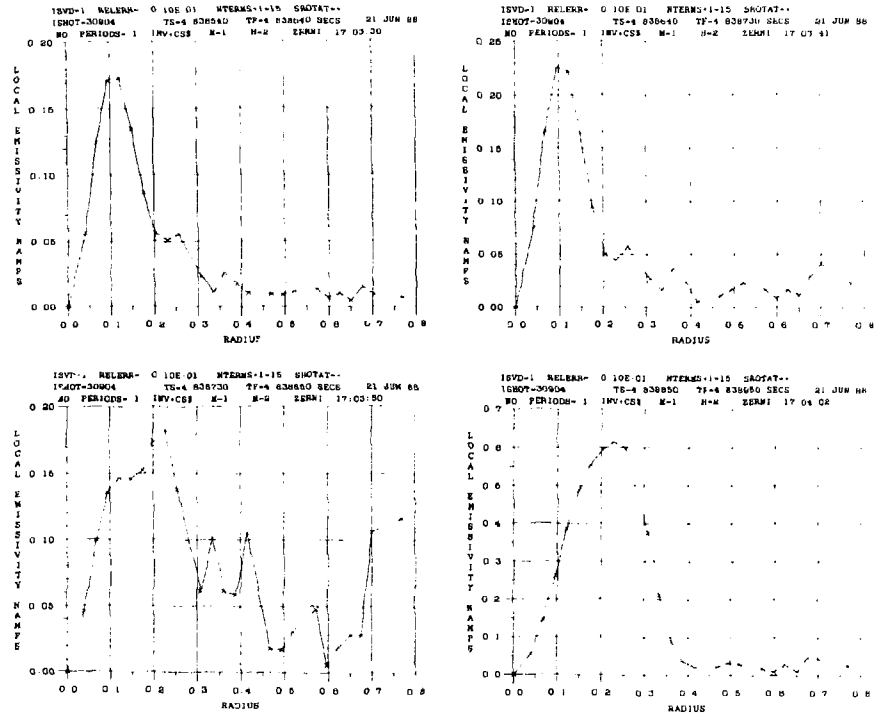
LOCAL EMISSIVITY WAMPS
RADIUS
0.00
0.05
0.10
0.15
0.20
0.25
0.0
0.1
0.2
0.3
0.4
0.5
0.6
0.7
0.8

Fig. 11a

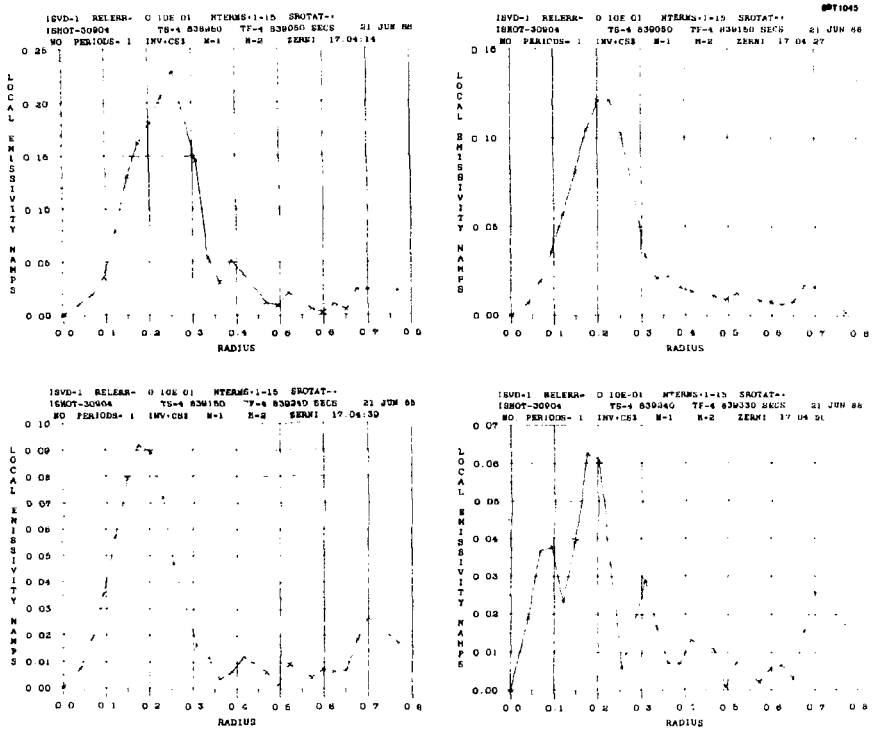
ISVD=1 RELERR= 0 10E 01 NTERMS=1=15 SROTAT=+
ISHOT=30904 TS=4 838850 TF=4 839050 SECS 21 JUN 88
NO PERIODS= 1 INV=CS1 M=1 N=2 ZERN1 17 04:14
LOCAL EMISSIVITY NAMPS
RADIUS
ISVD=1 RELERR= 0 10E 01 NTERMS=1=15 SROTAT=+
ISHOT=30904 TS=4 839050 TF=4 839150 SECS 21 JUN 88
NO PERIODS= 1 INV=CS1 M=1 N=2 ZERN1 17 04 27
LOCAL EMISSIVITY NAMPS
RADIUS
ISVD=1 RELERR= 0 10E 01 NTERMS=1=15 SROTAT=+
ISHOT=30904 TS=4 839150 TF=4 839240 SECS 21 JUN 88
NO PERIODS= 1 INV=CS1 M=1 N=2 ZERN1 17 04:39
LOCAL EMISSIVITY NAMPS
RADIUS
ISVD=1 RELERR= 0 10E 01 NTERMS=1=15 SROTAT=+
ISHOT=30904 TS=4 839240 TF=4 839330 SECS 21 JUN 88
NO PERIODS= 1 INV=CS1 M=1 N=2 ZERN1 17 04 51
LOCAL EMISSIVITY NAMPS
RADIUS

Fig. 11b

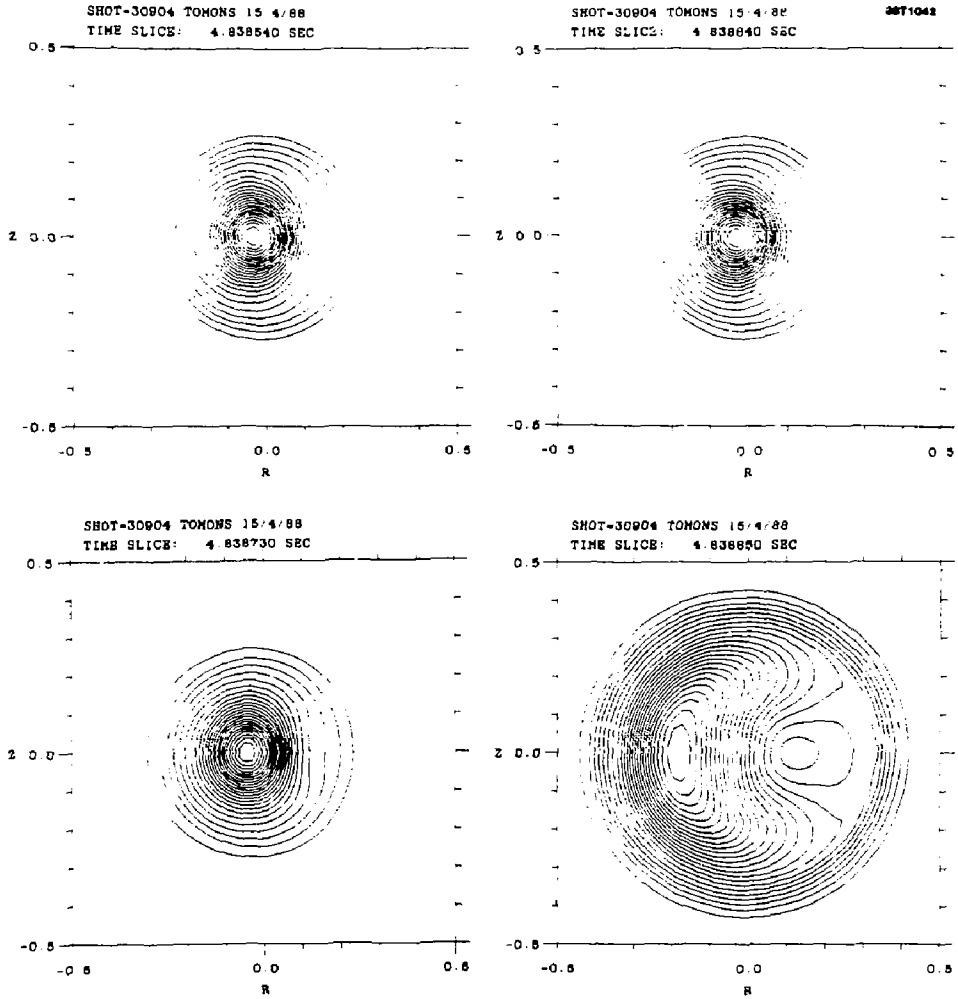
SHOT-30904 TOMONS 15 4/88
TIME SLICE: 4.838540 SEC
SHOT-30904 TOMONS 15/4/88
TIME SLICE: 4.838640 SEC
SHOT-30904 TOMONS 15/4/88
TIME SLICE: 4.838730 SEC
SHOT-30904 TOMONS 15/4/88
TIME SLICE: 4.838850 SEC
0.5
0.0
-0.5
Z
R

Fig. 12a

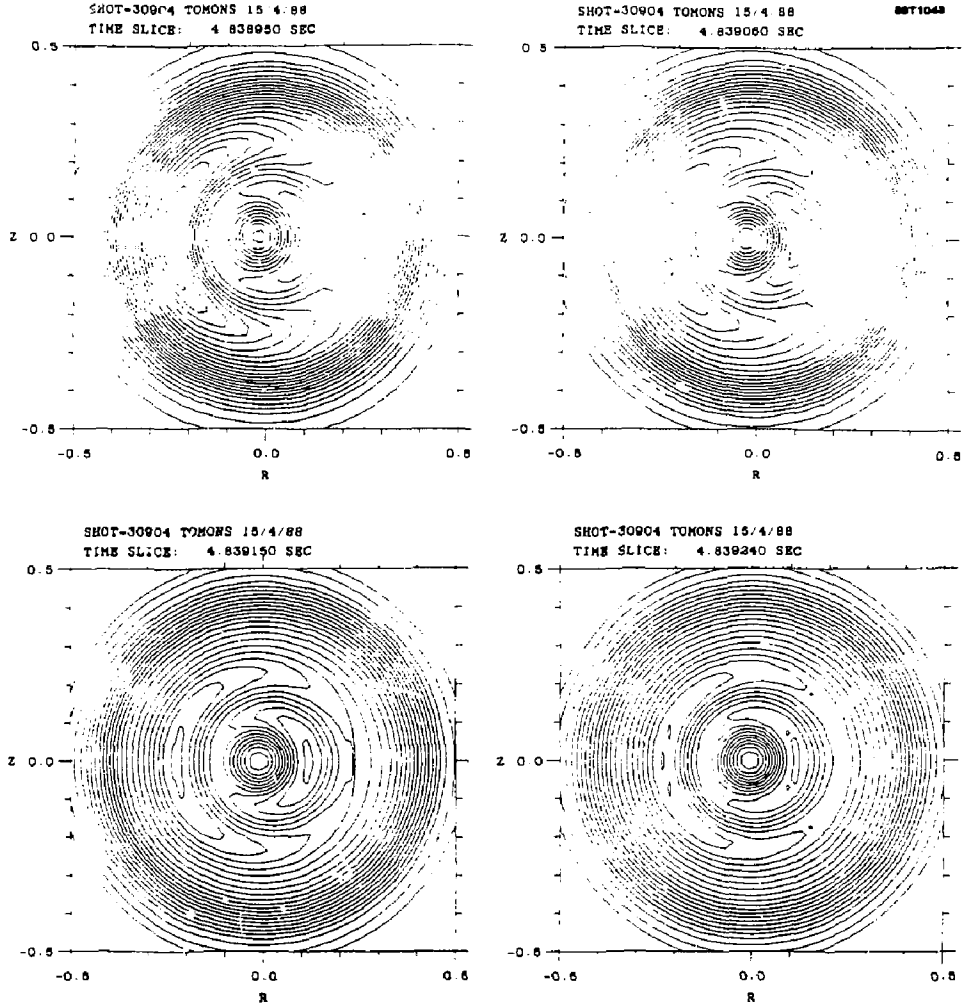
SHOT-30904 TOMONS 15 4 88
TIME SLICE: 4 838950 SEC
SHOT-30904 TOMONS 15/4 88
TIME SLICE: 4.839060 SEC
SHOT-30904 TOMONS 15/4/88
TIME SLICE: 4.839150 SEC
SHOT-30904 TOMONS 15/4/88
TIME SLICE: 4.839240 SEC
Z
R
0.5
0.0
-0.5

Fig. 12b

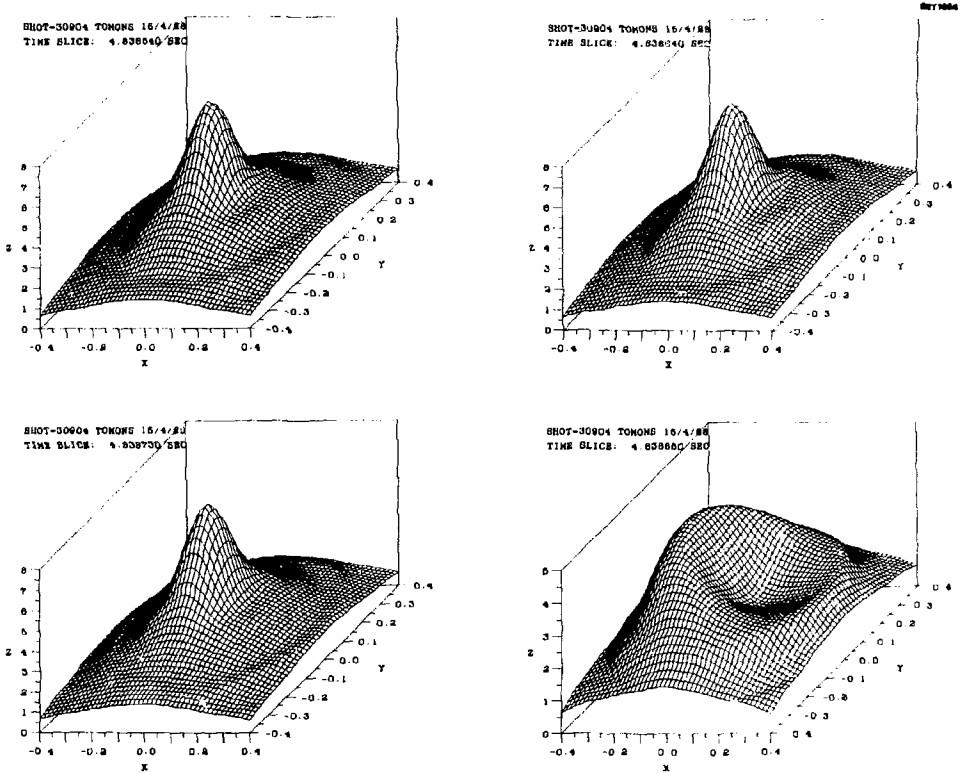
SHOT-30904 TOMONS 15/4/88
TIME SLICE: 4.838640 SEC
SHOT-30904 TOMONS 15/4/88
TIME SLICE: 4.838640 SEC
SHOT-30904 TOMONS 15/4/88
TIME SLICE: 4.838730 SEC
SHOT-30904 TOMONS 15/4/88
TIME SLICE: 4.838880 SEC
Z
X
Y

Fig. 13a

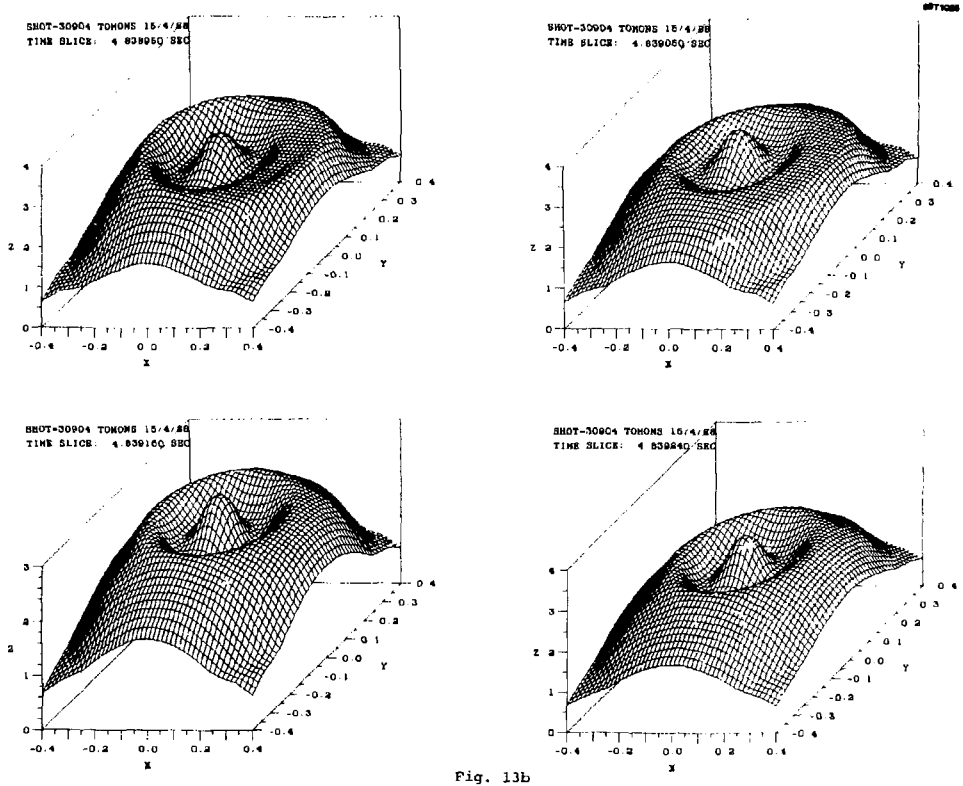
SHOT-30904 TOMOMS 15/4/88
TIME SLICE: 4.839050 SEC
SHOT-30904 TOMOMS 15/4/88
TIME SLICE: 4.839060 SEC
SHOT-30904 TOMOMS 15/4/88
TIME SLICE: 4.839160 SEC
SHOT-30904 TOMOMS 15/4/88
TIME SLICE: 4.839240 SEC
X
Y
Z

Fig. 13b

EXTERNAL DISTRIBUTION IN ADDITION TO UC-20

Dr. Frank J. Paoloni, Univ of Wollongong, AUSTRALIA
Prof. M.H. Brennan, Univ Sydney, AUSTRALIA
Plasma Research Lab., Australian Nat. Univ., AUSTRALIA
Prof. I.R. Jones, Flinders Univ., AUSTRALIA
Prof. F. Cap, Inst Theo Phys, AUSTRIA
Prof. M. Heindler, Institut fur Theoretische Physik, AUSTRIA
M. Goossens, Astronomisch Instituut, BELGIUM
Ecole Royale Militaire, Lab de Phys Plasmas, BELGIUM
Commission-European, Dg-XII Fusion Prog, BELGIUM
Prof. R. Boucique, Laboratorium voor Natuurkunde, BELGIUM
Dr. P.H. Sakanaka, Instituto Fisica, BRAZIL
Instituto De Pesquisas Espaciasi-INPE, BRAZIL
Documents Office, Atomic Energy of Canada Limited, CANADA
Dr. M.P. Bachynski, MPB Technologies, Inc., CANADA
Dr. H.M. Skarsgard, University of Saskatchewan, CANADA
Dr. H. Barnard, University of British Columbia, CANADA
Prof. J. Teichmann, Univ. of Montreal, CANADA
Prof. S.R. Sreenivasan, University of Calgary, CANADA
Prof. Tudor W. Johnston, INRS-Energie, CANADA
Dr. C.R. James, Univ. of Alberta, CANADA
Dr. Peter Lukac, Komanskeho Univ, CZECHOSLOVAKIA
The Librarian, Culham Laboratory, ENGLAND
The Librarian, Rutherford Appleton Laboratory, ENGLAND
Mrs. S.A. Hutchinson, JET Library, ENGLAND
C. Mouttet, Lab. de Physique des Milieux ionises, FRANCE
J. Radet, CEN/CADARACHE - Bat 506, FRANCE
Univ. of Ioannina, Library of Physics Dept. GREECE
Dr. Tom Mual, Academy Bibliographic Ser., HONG KONG
Preprint Library, Hungarian Academy of Sciences, HUNGARY
Dr. B. Dasgupta, Saha Inst of Nucl. Phys., INDIA
Dr. P. Kaw, Institute for Plasma Research, INDIA
Dr. Philip Rosenau, Israel Inst. Tech, ISRAEL
Librarian, Int'l Ctr Theo Phys, ITALY
Prof. G. Rostagni, Univ Di Padova, ITALY
Miss Clelia De Palo, Assoc EURATOM-ENEA, ITALY
Biblioteca, Instituto di Fisica del Plasma, ITALY
Dr. H. Yamato, Toshiba Res & Dev, JAPAN
Prof. I. Kawakami, Atomic Energy Res. Institute, JAPAN
Prof. Kyoji Nishikawa, Univ of Hiroshima, JAPAN
Direc. Dept. Large Tokamak Res. JAERI, JAPAN
Prof. Satoshi Itoh, Kyushu University, JAPAN
Research Info Center, Nagoya University, JAPAN
Prof. S. Tanaka, Kyoto University, JAPAN
Library, Kyoto University, JAPAN
Prof. Nobuyuki Inoue, University of Tokyo, JAPAN
S. Mori, JAERI, JAPAN
Librarian, Korea Advanced Energy Res. Institute, KOREA
Prof. D.I. Choi, Adv. Inst Sci & Tech, KOREA
Prof. B.S. Liley, University of Waikato, NEW ZEALAND
Institute of Plasma Physics, PEOPLE'S REPUBLIC OF CHINA
Librarian, Institute of Phys., PEOPLE'S REPUBLIC OF CHINA
Library, Tsing Hua University, PEOPLE'S REPUBLIC OF CHINA
Z. Li, Southwest Inst. Physics, PEOPLE'S REPUBLIC OF CHINA
Prof. J.A.C. Cabral, Inst Superior Tecnico, PORTUGAL
Dr. Octavian Petrus, AL I CUZA University, ROMANIA
Dr. Johan de Villiers, Fusion Studies, AEC, SO AFRICA
Prof. M.A. Hellberg, University of Natal, SO AFRICA
C.I.E.M.A.T., Fusion Div. Library, SPAIN
Dr. Lennart Stenflo, University of UMEA, SWEDEN
Library, Royal Inst Tech, SWEDEN
Prof. Hans Wilhelmson, Chalmers Univ Tech, SWEDEN
Centre Phys des Plasmas, Ecole Polytech Fed, SWITZERLAND
Bibliotheek, Fom-Inst Voor Plasma-Fysica, THE NETHERLANDS
Dr. D.D. Ryutov, Siberian Acad Sci, USSR
Dr. G.A. Eliseev, Kurchatov Institute, USSR
Dr. V.A. Glukhikh, Inst Electrophysical Apparatus, USSR
Dr. V.T. Tolok, Inst. Phys. Tech. USSR
Dr. L.M. Kovrizhnykh, Institute Gen. Physics, USSR
Nuclear Res. Establishment, Julich Ltd., W. GERMANY
Bibliothek, Inst. Fur Plasmaforschung, W. GERMANY
Dr. K. Schindler, Ruhr Universitat Bochum, W. GERMANY
ASDEX Reading Rm, IPP/Max-Planck-Institut fur Plasmaphysik, W. GERMANY
Librarian, Max-Planck Institut, W. GERMANY
Prof. R.K. Janev, Inst Phys, YUGOSLAVIA